Molecular-Level Insight into Selective Catalytic Reduction of NO$_x$ with NH$_3$ to N$_2$ over Highly Efficient Bifunctional V$_a$-MnO$_x$ Catalyst at Low Temperature

Ying Xin,[†] Hao Li,[†] Nana Zhang,[†] Qian Li,[†] Zhaoliang Zhang,*[†] Xiaoming Cao,*[‡] P. Hu,[‡]

Lirong Zheng,[§] and James A. Anderson*[∥]

[†]School of Chemistry and Chemical Engineering, Shandong Provincial Key Laboratory of Fluorine Chemistry and Chemical Materials, University of Jinan, Jinan 250022, China

[‡]Centre for Computational Chemistry and Research Institute of Industrial Catalysis, School of Chemistry and Molecular Engineering, East China University of Science and Technology, Shanghai 200237, China

[§]Institute of High Energy Physics, Chinese Academy of Sciences, Beijing 100049, China

[∥]Surface Chemistry and Catalysis Group, Materials and Chemical Engineering, University of Aberdeen, AB24 3UE, United Kingdom

17 **ABSTRACT**: Selective catalytic reduction of NO_x with ammonia (SCR) is not only an important

18 model catalytic reaction, but also significant in terms of improving environmental air quality and

19 human health. However, SCR catalysts suffer from the low activity and selectivity to N_2 at low

20 temperature, which in part may be attributed to our limited understanding of the reaction

21 mechanism. Here, an unambiguous molecular-level mechanism is presented for an improved

22 low-temperature SCR activity using the bifunctional catalysts composed of highly active oxides

23 (Mn_2O_3) for NH_3 activation and highly selective vanadates ($Mn_2V_2O_7$) which promote N_2

24 formation. NH_3 is initially activated by Mn_2O_3 to form an NH_2 intermediate. Transfer of NH_2 to

25 $Mn_2V_2O_7$ then takes place which facilitates the capture of gaseous NO leading to the formation

26 of NH_2NO over $Mn_2V_2O_7$, whereafter NH_2NO is efficiently converted to the preferred N_2 rather

27 than the undesired by-product, N_2O. The proximity of the two components achieved *via* sol-gel

28 preparation plays a crucial role in the transfer of active intermediates.

29

32

1. INTRODUCTION

34   As one of the main fields of interest in environmental catalysis, nitrogen oxides (NO_x) removal

35 using catalytic technologies has always received significant attention from researchers.[1]

36 Selective catalytic reduction (SCR) of NO_x with ammonia (NH_3) is considered as the most

37 efficient and widely used technology, however, developing the low-temperature active catalyst

38   (< 200°C) with high N_2 selectivity still remains a challenge.[2,3] In general, the adsorption and

39   activation of NH_3 on the acid sites of the catalysts is regarded as a key step in SCR reaction to

40   enable NO_x conversion at low temperatures.[4,5] Furthermore, the activation of adsorbed NH_3

41   relies on an oxidizing component such as a transition metal oxide.[6-8] However, N_2 selectivity is

42   exceptionally low while employing catalysts with adequate oxidation capability, such as Mn

43   oxides (MnO_x).[2,3,9] MnO_x catalysts permit the high NO_x conversion at low temperature, while the

44   selectivity to N_2 decreases due to the excessive activation of N-H bond and the resultant

45   oxidation of NH_3 by NO, gaseous O_2 and bulk O.[3,10] Although the activity of MnO_x catalysts can

46   be modified by changing the Mn oxidation state,[11] crystallinity,[3,12] as well as the surface area and

47   morphology,[13] the low N_2 selectivity is still an inevitable drawback which must be overcome for

48   the practical applications.[2,9,10]

49   In general, two plausible strategies have been adopted to enhance the low-temperature SCR

50   performance of MnO_x catalysts.[2,9,10,14] One strategy is to synthesize bi- or multi-metal oxide

51   catalysts to construct specific active sites which combine MnO_x with other metal oxides (Fe,[15]

52   Ce,[16-18] Ni,[19] Nb,[20] Cr,[21] Zr,[22] etc.), or supported MnO_x on TiO_2,[23-26] SiO_2,[25,27] Al_2O_3,[25,28,29]

53   zeolites[30-32], and carbon-based materials.[33-36] The improved activity and N_2 selectivity were thus

54   achieved. The second approach is to prepare materials to develop the bifunctional catalysts,

55   which involve the cooperation of two types of active sites with specific properties.[37-41] Several

56   bifunctional catalysts that consist of an oxidation component (such as Mn, Mn-Ce, Mn-Cr, Mn-

57   Cu, Mn/Ce-Zr oxides,[38,39,42] CoO_x-CuO_x/TiO_2,[43] etc.) and an SCR-active component (such as Fe-

58   ZSM-5,[38,39] V_2O_5-WO_3/TiO_2,[39] Fe-beta,[42] $NiMn_2O_4$,[43] etc.) have received attention, in which V-

59   based oxides possess high N_2 selectivity and resistance to sulfur oxide poisoning.[44,45]

60   Specifically, vanadates attract intensive attention due to the higher thermal stability than V_2O_5.[46-

61 [50] However, vanadates have not been exploited to date as an active component of a bifunctional

62 SCR catalyst.[46,47,49,51,52] Furthermore, the deceptively simple synergism between the oxidation

63 component and the SCR-active component for the bifunctional catalysts still remains elusive at a

64 molecular level.[53] For instance, Salazar et al. found that such a synergy completely vanished

65 when the two components present as separate beds of an oxidation catalyst and an SCR catalyst.

66 On this basis, they challenged the so-called "fast SCR" route and proposed a possible HNO_2

67 intermediate which may be formed over the oxidation component and proceeds to the SCR sites

68 for further reaction. However, no spectroscopic or simulated/computed evidence was

69 presented.[39]

70   In the present work, a Mn-V composite oxide (V_a-MnO_x) composed of NH_3 activation

71 component (Mn_2O_3) and N_2 formation component ($Mn_2V_2O_7$) was prepared to probe the intrinsic

72 SCR mechanism at low temperature from both an experimental and theoretical basis. Mn_2O_3 was

73 confirmed to activate adsorbed NH_3 into a weakly adsorbed intermediate, NH_2, which can be

74 transferred to $Mn_2V_2O_7$, where it reacts with the gaseous NO to form NH_2NO. The selective

75 decomposition of NH_2NO into N_2 is far more favorable over $Mn_2V_2O_7$ than on Mn_2O_3. As a

76 result, both the high activity and high N_2 selectivity are achieved over the bifunctional V_a-MnO_x

77 catalyst at low temperature. This demonstrates a significant progress in balancing activity and

78 selectivity of the two aspects of MnO_x-based SCR catalysts.

79

80 **2. EXPERIMENTAL SECTION**

81   **Catalyst preparation.** A series of V_a-MnO_x catalysts were prepared by a sol-gel method. A

82 known amount of NH_4VO_3, $Mn(CH_3COO)_2$ and citric acid (CA) were mixed together in a

83   specific order with designated molar ratios. NH_4VO_3 was dissolved in 30 mL purified water at

84   70^oC in a water bath under vigorous stirring, until the NH_4VO_3 had been fully dissolved and then

85   held there for about 30 min. The corresponding quantity of CA was then slowly added to the

86   solution and held for 30 min. The molar ratio of citric acid to the metal components (the total

87   moles of vanadium and manganese) was fixed at 1.0. After that, the $Mn(CH_3COO)_2$ was added to

88   the solution and stirred for 2 h. The suspension obtained was transferred to an evaporating dish

89   and oven dried at 110^oC overnight. The resulting materials were calcinated at 450^oC for 5 h in

90   muffle furnace in static air. The mixed oxides were denoted as V_a-MnO_x, where a represents the

91   molar ratios of V/(V+Mn). Pure manganese oxide and vanadium-based oxide were synthesized

92   using a similar procedure. For comparison and further investigation, oxidation phase (Mn_2O_3)

93   and reactive phase ($Mn_2V_2O_7$) components were mechanically mixed with the $Mn_2V_2O_7$ to yield

94   a materials consistent with $V_{0.05}$-MnO_x, and denoted as Mn_2O_3+$Mn_2V_2O_7$. Another reference

95   sample denoted as MoO_3+$Mn_2V_2O_7$ was also synthesized by a similar procedure. Before SCR

96   activity tests, the catalysts were pressed, crushed and sieved to 40-60 mesh.

97   **Catalyst characterization.** X-ray diffraction (XRD) patterns of the samples were recorded on

98   a Bruker D8-FOCUS X-ray diffractometer using Cu Kα radiation (λ = 1.5418 Å) at 50 kV and

99   30 mA. Intensity data were collected over a 2θ range of 10-80° with a 0.03^o step size and a

100   counting time of 0.3 s per point. The relative amount of various components in V_a-MnO_x can be

101   obtained using the quantitative XRD analysis by the reference intensity ratio (RIR) method.[54]

102   Inductively coupled plasma-atomic emission spectrometer (ICP-AES) experiments were carried

103   out on the IRIS Intrepid IIXSP instrument from Thermo elemental. Transmission electron

104   microscopy (TEM) was conducted using a JEOL JEM-2010 microscope at an accelerating

105   voltage of 200 kV. X-ray photoelectron spectroscopy (XPS) data were obtained on an Escalab

250Xi instrument from Thermo Fisher Scientific using monochromatic Al Kα radiation. To compensate for surface charging effects, the binding energies were calibrated using the C 1s hydrocarbon peak at 284.80 eV. X-ray absorption fine structure (XAFS) measurements at the Mn and V K-edges were performed in the transmission and fluorescence modes, respectively, at room temperature on the XAFS station of the 1W1B beam line of Beijing Synchrotron Radiation Facility (BSRF, Beijing, China), respectively. XAFS data were analyzed using the IFEFFIT software package.[55] Brunauer-Emmett-Teller (BET) surface areas were determined from N_2 adsorption/desorption isotherms using a Micromeritics ASAP2020M instrument. Before exposure to N_2, samples were outgassed at 300^oC for 5 h. Raman spectroscopy was obtained using a RM2000 (RENISHAW) with the 532 nm laser line. H_2-temperature programmed reduction (H_2-TPR) experiments were carried out on a TP-5000 Multifunctional Adsorption Instrument with a thermal conductivity detector (TCD) to monitor H_2 consumption. Before testing, 50 mg of sample was sieved to 40-60 mesh and pretreated at 400^oC for 30 minutes in a 30 mL/min flow of pure O_2, then cooled to room temperature in the same atmosphere. The reduction temperature was raised at 10^oC/min from 30 to 800^oC in a 30 mL/min flow of 5 vol.% H_2 in N_2. In order to quantify the total amount of H_2 consumed, a CuO standard was used for calibration purposes. NH_3-temperature programmed desorption (NH_3-TPD) experiments were performed in a quartz reactor using 50 mg of catalyst. NH_3 (m/z=16) was monitored using a quadrupole Mass Spectrometer (OmniStar 200, Balzers). Prior to experiment, the samples were pretreated at 400^oC for 30 min in 10 vol.% O_2/He (50 mL/min) and then cooled to 30^oC. NH_3 adsorption was performed in 4000 ppm NH_3 (50 mL/min) until the outlet NH_3 concentration remained constant. Samples were then purged with pure He for 1 h to remove weakly bound NH_3. Finally, the samples were heated to 500^oC at 10^oC/min. *In situ* infrared (IR) spectra were

129   recorded using a Bruker Tensor 27 spectrometer over the range 4000-400 cm^{-1}, with 16 scans, at

130   a resolution of 4 cm^{-1}. Self-supporting wafers were pretreated in the cell at 400°C in a flow of He

131   for 30 min to remove any adsorbed species. After cooling to ambient temperature, a background

132   spectrum was recorded. The IR spectra were recorded at room temperature in a flow of 500 ppm

133   NH_3+He balance or 500 ppm NH_3+500 ppm NO+5.3 vol.% O_2+He balance (150 mL/min). The

134   samples were then heated to 250°C at 10°C/min.

135   **Catalytic activity.** The steady state SCR activity over V_a-MnO_x catalysts and the reference

136   samples were tested in a fixed-bed quartz tube reactor (6.0 mm i.d.) with a thermocouple placed

137   inside the catalyst bed in the temperature range 150-450°C. In SCR reactions, the model flue gas

138   consisted of 500 ppm NO, 500 ppm NH_3, 5.3 vol.% O_2 and He balance. The total flow rate was

139   maintained at 300 mL/min corresponding to a gas hourly space velocity (GHSV) of 50 000 h^{-1}.

140   Concentrations of NO and NO_2 were monitored by a chemiluminiscence NO_x analyzer (42i-HL,

141   Thermo). N_2O and NH_3 were determined by quadrupole mass spectrometer (MS, OmniStar 200,

142   Balzers) using the m/z of 44 for N_2O, and 17 for NH_3. The data for steady-state activity of

143   catalysts were collected after about 1 h on stream. From the concentration of the gases at steady

144   state, the NO_x conversion and N_2 selectivity were calculated according to the following

145   equations:

146
$$NO_x \text{ conversion } (\%) = \frac{[NO_x]_{in} - [NO_x]_{out}}{[NO_x]_{in}} \times 100\%$$

147
$$N_2 \text{ selectivity } (\%) = \frac{[NO_x]_{in} + [NH_3]_{in} - [NO_x]_{out} - [NH_3]_{out} - 2[N_2O]}{[NO_x]_{in} + [NH_3]_{in} - [NO_x]_{out} - [NH_3]_{out}} \times 100\%$$

148   By assuming conditions free from diffusion limitations were met, the SCR reaction rates

149   normalized by sample mass and BET surface area of the catalyst can be calculated according to

150   the following equation:[4]

151
$$\text{Rate} = \frac{X_{NO}QC_f}{V_m W(S_{BET})}$$

152   where X_{NO} is the NO conversion at a steady SCR reaction temperature (100 ^{o}C) (%), Q is the

153   volumetric flow rate (300 mL/min) and C_f is the feeding concentration of NO (500 ppm). V_m is

154   the molar volume of gas (22.4 mL/mol), W is the sample weight (g) and S_{BET} is the BET surface

155   area of the catalyst (m^2/g).

156

3. THEORETICAL CALCULATIONS

158   To understand the relevant structural and electronic properties of Mn_2O_3 and $Mn_2V_2O_7$

159   materials and the SCR network occurring on their surfaces at a molecular level, the spin

160   polarized first-principles calculations based on density functional theory (DFT) implemented in

161   the Vienna *ab initio* Software Package (VASP)[56,57] were performed with a plane-wave kinetic

162   energy cutoff of 500 eV. The projector augmented wave (PAW) pseudo potentials[58] were utilized

163   to describe the valence-core interactions. The exchange-correlated term was described utilizing

164   generalized gradient approximation (GGA) of Perdew-Burke-Ernzerhoff (PBE).[59] The PBE+U

165   approach was also used to address the on-site Coulomb interactions in the localized d orbitals of

166   Mn and V cations through an additional Hubbard-type U term.

167   For Mn_2O_3, since it will be converted from orthorhombic structure (space group *Pcab*) to

168   cubic structure (space group *Ia3*) in the form of α phase once the temperature is above 308 K[60]

169   which is lower than the SCR reaction temperature, a cubic conventional unit cell of α-Mn_2O_3

170   containing 16 units of Mn_2O_3 with the equilibrium lattice constant of 9.658 Å was investigated.

171   The effective $U = 4.0$ eV fitted according to its oxidation energy[61] was utilized for the Mn cation

172   at α-Mn_2O_3. The exposed Mn_2O_3(202) surface found by TEM was modeled by a 4-layer $p(1\times1)$

173   slab of 8.364 Å $\times$ 8.364 Å separated by a ~10 Å vacuum in Z direction utilizing $4 \times 4 \times 1$ k-point

174   mesh for Brillouin integration.

175     $Mn_2V_2O_7$ exists in the form of β-$Mn_2V_2O_7$ with a thortveitite-like structure in a monoclinic

176   system of space group $C2/m$ at the reaction temperature.[62] Hence, the bulk β-$Mn_2V_2O_7$

177   containing 2 $Mn_2V_2O_7$ units within a unit cell of 6.710 Å $\times$ 8.726 Å $\times$4.970 Å was modeled as

178   the most stable ferromagnetic (FM) states.[63] The effective $U = 4.0$ and 3.1 eV as reported for

179   isovalent binary metal oxides[61] were utilized for Mn and V, respectively. For the exposed

180     $Mn_2V_2O_7$($\bar{2}$01) surface, there are two possible terminations. The only difference between

181     $Mn_2V_2O_7$($\bar{2}$01)-A and $Mn_2V_2O_7$($\bar{2}$01)-B terminals is the existence of the exposed one-fold

182   coordinated oxygen anion (O_{1c}). The more stable $Mn_2V_2O_7$($\bar{2}$01)-A terminal with O_{1c} was

183   studied during this reaction. We refer to $Mn_2V_2O_7$($\bar{2}$01)-A as $Mn_2V_2O_7$($\bar{2}$01) hereinafter. The

184   stoichiometric exposed β-$Mn_2V_2O_7$($\bar{2}$01) surface was modeled by a 6-layer $p(1\times1)$ slab of 6.868

185   Å $\times$6.868 Å separated by a ~10 Å vacuum in Z direction utilizing $4 \times 4 \times 1$ k-point mesh for

186   Brillouin integration.

187   For both Mn_2O_3(202) and $Mn_2V_2O_7$($\bar{2}$01) surfaces, during the geometry optimization, the

188   bottom two layers were fixed while the adsorbates and the other layers were relaxed until the

189   force of each atom was lower than 0.05 eV/Å. The transition states (TSs) were determined within

190   a constrained minimization scheme with the same force convergence criterion.[64-66] Each TS was

191   further verified as the first-order saddle with only one imaginary vibrational frequency and the

192   corresponding vibrational mode along the reaction coordination based on the numerical

193   vibrational frequency analysis.

194   The adsorption energies of reactants were calculated following:

195
$$E_{ad}(x) = E(slab) + E(x) - E(x/\text{slab})$$

196   where $E(slab)$, $E(x)$ and $E(x/\text{slab})$ are the total energies of the catalyst surface, x in the gas phase

197   and x adsorbed on the catalyst surface, respectively. The more positive $E_{ad}(x)$ is, the more

198   strongly the species x binds with the surface. The adsorption energies were also checked utilizing

199   the screened hybrid functional of Heyd-Scuseria-Ernzerhoff functional (HSE06)[67] at the

200   optimized structure obtained from PBE+U level.

201

202   4. RESULTS AND DISCUSSION

203   4.1 Structural characterization and catalytic activity

204
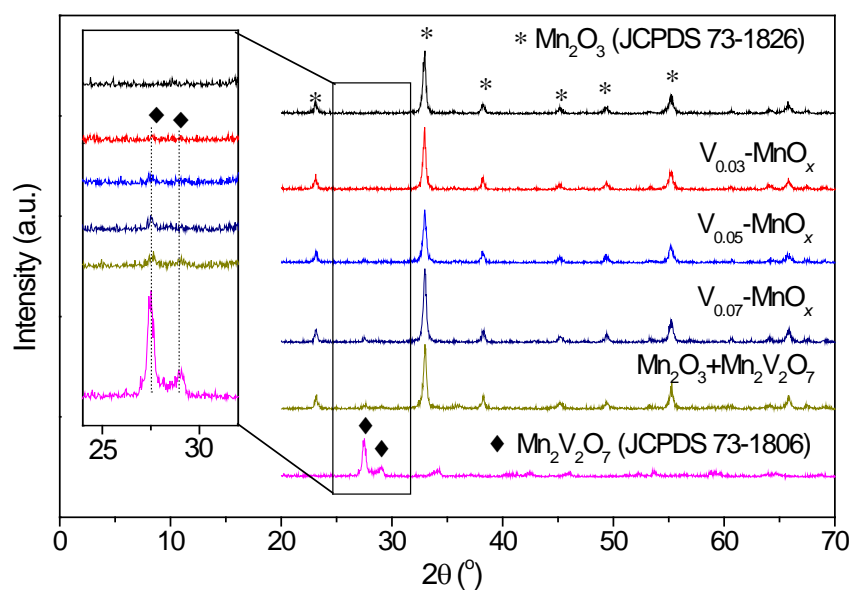
Figure 1. XRD patterns of V_a-MnO$_x$, Mn$_2$O$_3$, Mn$_2$V$_2$O$_7$ and reference samples.

206

207   **Table 1.** ICP, XRD, XPS, surface areas, H$_2$-TPR, and NH$_3$ desorption data for V_a-MnO$_x$.

| Samples	ICP data			Theoretical values		XRD		XPS		Surface area (m^2/g)	H$_2$-uptake (µmol/g)	NH$_3$ desorption		
	V (wt.%)	Mn (wt.%)	V/Mn molar ratio	V/Mn molar ratio	Mn$_2$V$_2$O$_7$ (wt.%)	Mn$_2$V$_2$O$_7$ (wt.%)	Mn$_2$O$_3$/ Mn$_2$V$_2$O$_7$ molar ratio	Surface V/Mn molar ratio	O$_\alpha$/(O$_\alpha$+O$_\beta$) (%)			(µmol/g)	(µmol/m^2)	Theoretical (µmol/m^2)
Mn$_2$O$_3$	--	68.59	--	--	0	0	0	0	35.7	31.9	1128	27.01	0.85	0.85
V$_{0.03}$-MnO$_x$	1.53	65.49	0.03	0.03	6.0	4.7	32.1	0.03	33.9	28.9	1209	37.32	1.29	0.93
V$_{0.05}$-MnO$_x$	2.64	63.90	0.04	0.05	10.2	10.4	18.1	0.05	34.7	39.2	1239	47.72	1.22	1.00
V$_{0.07}$-MnO$_x$	3.77	64.75	0.06	0.07	14.3	14.2	12.3	0.05	32.5	32.3	1062	40.61	1.26	1.06
Mn$_2$V$_2$O$_7$	33.67	34.95	1.03	1	100	100	--	0.69	22.2	15.5	1125	35.62	2.29	2.29
Mn$_2$O$_3$+ Mn$_2$V$_2$O$_7$	3.06	67.36	0.05	0.05	10.2	10.0	18.5	0.67	24.3	31.1	1332	--	--	--

208

209   XRD patterns show that V_a-MnO$_x$ composite oxides contain Mn$_2$O$_3$ (JCPDS No. 73-1826,

210   orthorhombic) and Mn$_2$V$_2$O$_7$ (JCPSD No. 73-1806, monoclinic) phases (Figure 1). The contents

211   of Mn$_2$V$_2$O$_7$ from the quantitative XRD analysis coincide with the theoretical values and ICP

212   data, indicating that the doped V might exist in the form of Mn$_2$V$_2$O$_7$ (Table 1). On the basis of

213   the similar Mn K-edge X-ray absorption near edge structure (XANES) spectra and radial

214   structure function (RSF) curves for Mn$_2$O$_3$ and V_a-MnO$_x$ (Figure S1), most of the Mn atoms in

215   V_a-MnO$_x$ are trivalent and in octahedral coordination, and others are in the form of Mn$_2$V$_2$O$_7$

216   according to XRD (Figure 1). On the other hand, two peaks are recognized at ~1.7 Å and ~3.1 Å

in the RSF curves of $Mn_2V_2O_7$, corresponding to the Mn^{2+}-O and Mn^{2+}-V shells, respectively. In the case of the V K-edge, the peak position and shape of the normalized XANES and RSF (Figure 2) curves for V_a-MnO_x correspond well with those of $Mn_2V_2O_7$ and $Mn_2O_3+Mn_2V_2O_7$, consistent with the XRD patterns (Figure 1 and Table 1) confirming that all of the V atoms in V_a-MnO_x exist in the same tetrahedral coordination environment as in $Mn_2V_2O_7$.[68] Raman spectra also show the $Mn_2V_2O_7$ phase for $V_{0.07}$-MnO_x (Figure S2).
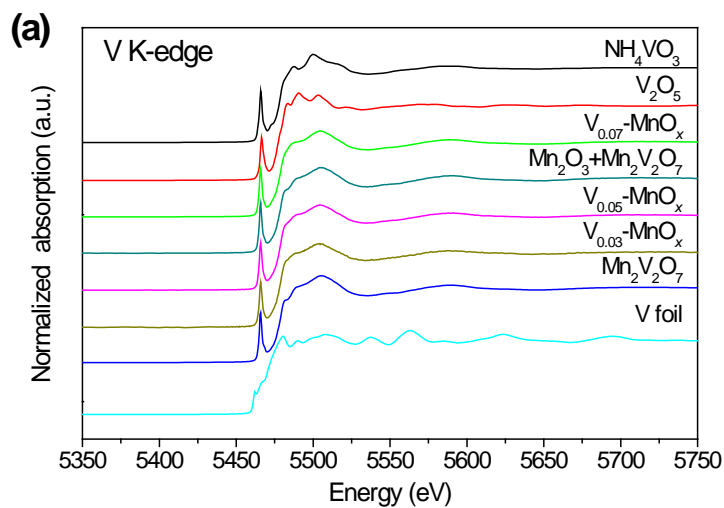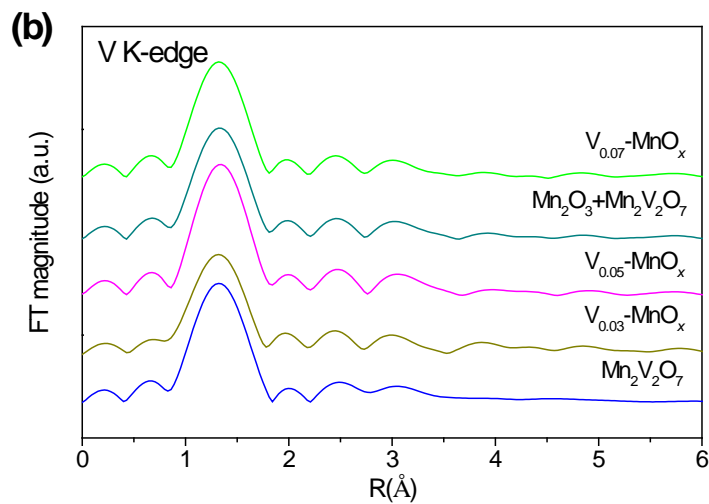
226　　**Figure 2.** Normalized XANES spectra (a) and the RSF curves (b) of V K-edge for V_a-MnO$_x$ and

227　　　　　　　　　　　　　　　the reference samples.

228

229　　　XPS was further used to characterize the surfaces of V_a-MnO$_x$. For Mn$_2$O$_3$ and V_a-MnO$_x$, no

230　　obvious change in binding energies of Mn 2p was observed due to the excess Mn$_2$O$_3$ in V_a-MnO$_x$

231　　(Figure S3a). As for Mn$_2$V$_2$O$_7$, the Mn 2p$_{3/2}$ binding energy was located at 640.8 eV, which is

232　　attributed to Mn^{2+}.[7] Compared with those of Mn$_2$V$_2$O$_7$ and Mn$_2$O$_3$+Mn$_2$V$_2$O$_7$, the binding

233　　energies of V 2p for V_a-MnO$_x$ show an obvious shift toward lower values, indicating a reduction

234　　in the oxidation state of V,[69,70] probably due to the the strong interaction between Mn$_2$O$_3$ and

235　　Mn$_2$V$_2$O$_7$ (Figure S3b). The O 1s peaks can be fitted using two oxygen species, the lattice

236　　oxygen at ∼529.9 eV (O$_\beta$) and the chemisorbed surface oxygen at ∼531.1 eV (O$_\alpha$) (Figure S3c).[7]

237　　The close values of [O$_\alpha$/(O$_\alpha$+O$_\beta$)] for V_a-MnO$_x$ to Mn$_2$O$_3$, which are much higher than those in

238　　Mn$_2$V$_2$O$_7$ and Mn$_2$O$_3$+Mn$_2$V$_2$O$_7$, guarantee the activiton of NH$_3$ on V_a-MnO$_x$. The approximate

239　　V/Mn atomic ratio of V_a-MnO$_x$ to ICP and theoretical values also suggest that V is not enriched

240　　on the surface.

241

242

243
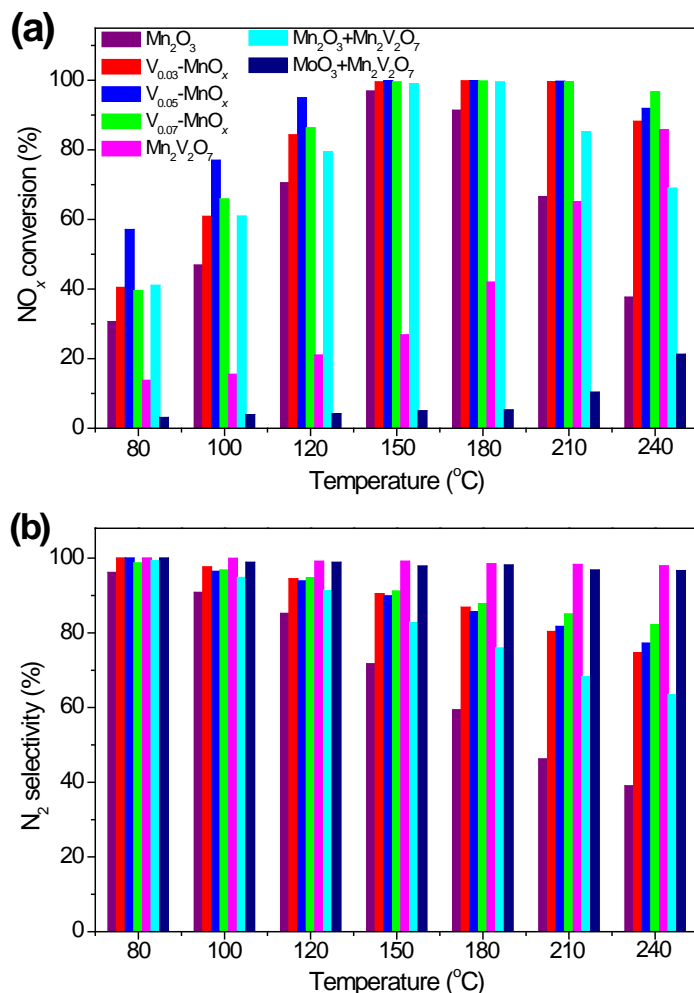
Figure 3. (a) NO$_x$ conversion and (b) N$_2$ selectivity for V$_a$-MnO$_x$, Mn$_2$O$_3$, Mn$_2$V$_2$O$_7$ and reference samples.

244

245

246

247   NO conversion and selectivity to N$_2$ are shown in Figure 3. Mn$_2$O$_3$ is active in SCR reaction

248   over the whole temperature range, however, N$_2$ selectivity decreases significantly with

249   increasing temperature. In contrast, Mn$_2$V$_2$O$_7$ exhibits much lower activity with excellent N$_2$

250   selectivity. Evidently, both NO$_x$ conversion and N$_2$ selectivity were improved for V$_a$-MnO$_x$. In

251   particular, V$_{0.05}$-MnO$_x$ shows NO$_x$ conversions above 90% between 120 and 240°C, and the N$_2$

252   selectivity was always above 80%. Furthermore, NO$_x$ conversion to N$_2$ for V$_{0.05}$-MnO$_x$ is higher

than that of the $Mn_2O_3+Mn_2V_2O_7$ sample, which constitutes the arithmetic sum of individual components with the same component content as $V_{0.05}$-MnO_x, at measured temperatures, suggesting the existence of synergism between Mn_2O_3 and $Mn_2V_2O_7$ in $V_{0.05}$-MnO_x. However, if Mn_2O_3 is replaced by an equivalent non-oxidant MoO_3, NO_x conversion is even lower than that of $Mn_2V_2O_7$, confirming that the presence of Mn_2O_3 is indispensable for the reaction. Moreover, the samples did not undergo structural modifications during the SCR reactions (Figure S4).
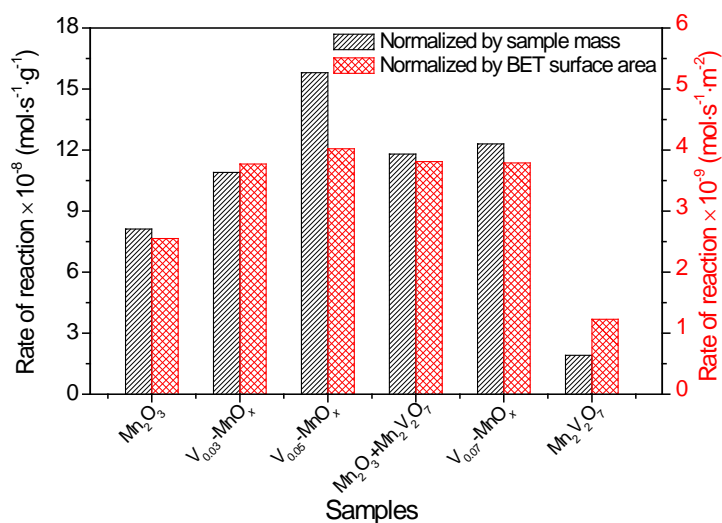
**Figure 4.** Reaction rates at $100^{\circ}C$ for V_a-MnO_x, Mn_2O_3, $Mn_2V_2O_7$ and reference samples.

Figure 4 shows the reaction rates for NO_x conversion to N_2 in the kinetic regime at $100^{\circ}C$. The activity for N_2 production is improved over V_a-MnO_x on the basis of the specific rate per gram and per surface area, and $V_{0.05}$-MnO_x is the most active for N_2 production. Furthermore, the $Mn_2O_3+Mn_2V_2O_7$ sample shows similar behavioral trends but to a less extent than $V_{0.05}$-MnO_x.

267 This again indicates that the improved activity of V_a-MnO$_x$ has a basis in the synergism between

268 Mn$_2$O$_3$ and Mn$_2$V$_2$O$_7$.

269

270 **4.2 Redox and acid properties**

271
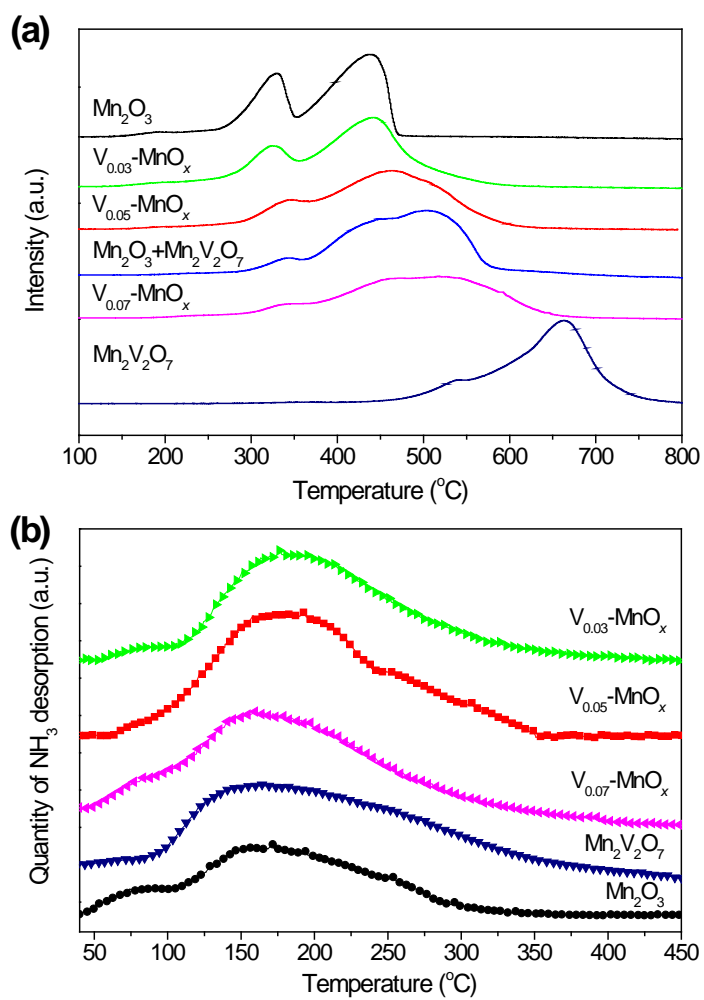
272

273

274 **Figure 5.** (a) H$_2$-TPR profiles for Mn$_2$O$_3$, Mn$_2$V$_2$O$_7$, V_a-MnO$_x$ and reference samples, and (b)

275 NH$_3$-TPD profiles of Mn$_2$O$_3$, Mn$_2$V$_2$O$_7$, and V_a-MnO$_x$.

276

16

277   Mn-based catalysts have been reported to show the improved SCR activity due to their strong

278   redox properties.[10] Hence, H_2-TPR patterns of V_a-MnO_x (and references) were performed

279   (Figure 5a). Based on the XRD patterns of the samples after SCR reactions (Figure S5), the

280   reduction products of Mn_2O_3 and $Mn_2V_2O_7$ are MnO and MnV_2O_4, respectively. Mn_2O_3 shows

281   peaks at 328 and 440°C, which are assigned to the reduction of Mn_2O_3 to Mn_3O_4 and Mn_3O_4 to

282   MnO, respectively. $Mn_2V_2O_7$ shows only a high-temperature reduction peak above 500°C,

283   corresponding to the transformation, V^{5+} ($Mn_2V_2O_7$) to V^{3+} (MnV_2O_4). The low-temperature

284   redox peaks of V_a-MnO_x could be attributed to the reduction of Mn species. However, compared

285   with pure Mn_2O_3 and $Mn_2V_2O_7$, the Mn^{3+} reduction to Mn^{2+} is shifted to higher temperature

286   while the reduction of V^{5+} into V^{3+} starts at a lower temperature in V_a-MnO_x, suggesting

287   synergistic effects between Mn_2O_3 and $Mn_2V_2O_7$ in V_a-MnO_x possibly involving H spillover

288   from Mn_2O_3 to $Mn_2V_2O_7$, which results in the simultaneously suppression of Mn^{3+} reduction and

289   promotion of the V^{5+} reduction. In addition, the primarily quantitive H_2 consumption is very

290   close (Table 1).

291   Acidity is another crucial factor in SCR reactions.[71] To determine this aspect of these samples,

292   NH_3-TPD was carried out (Figure 5b) and the corresponding desorption quantities were

293   calculated (Table 1). More NH_3 was desorbed from V_a-MnO_x compared with Mn_2O_3, $Mn_2V_2O_7$,

294   and the theoretical mass-weighted arithmetic values calculated from the corresponding weight

295   ratio of Mn_2O_3 and $Mn_2V_2O_7$ in V_a-MnO_x, which would be consistent with synergistic effects

296   arising between Mn_2O_3 and $Mn_2V_2O_7$ for the V_a-MnO_x samples. In addition, the temperature

297   range of NH_3 desorption is consistent with the active temperature window for SCR of V_a-MnO_x.

298   The maximum NH_3 desorption per gram sample was obtained for $V_{0.05}$-MnO_x which also shows

299   the highest reaction rate (Table 1 and Figure 4). However, the NH_3 desorption amount per unit

300 surface area of V_a-MnO$_x$ was nearly identical (Table 1), suggesting that the promoted SCR

301 performance of V_a-MnO$_x$ originate from the increased acid amounts in despite of their various

302 compositions.

303

304 **4.3 *In situ* IR spectra of NH$_3$ adsorption**
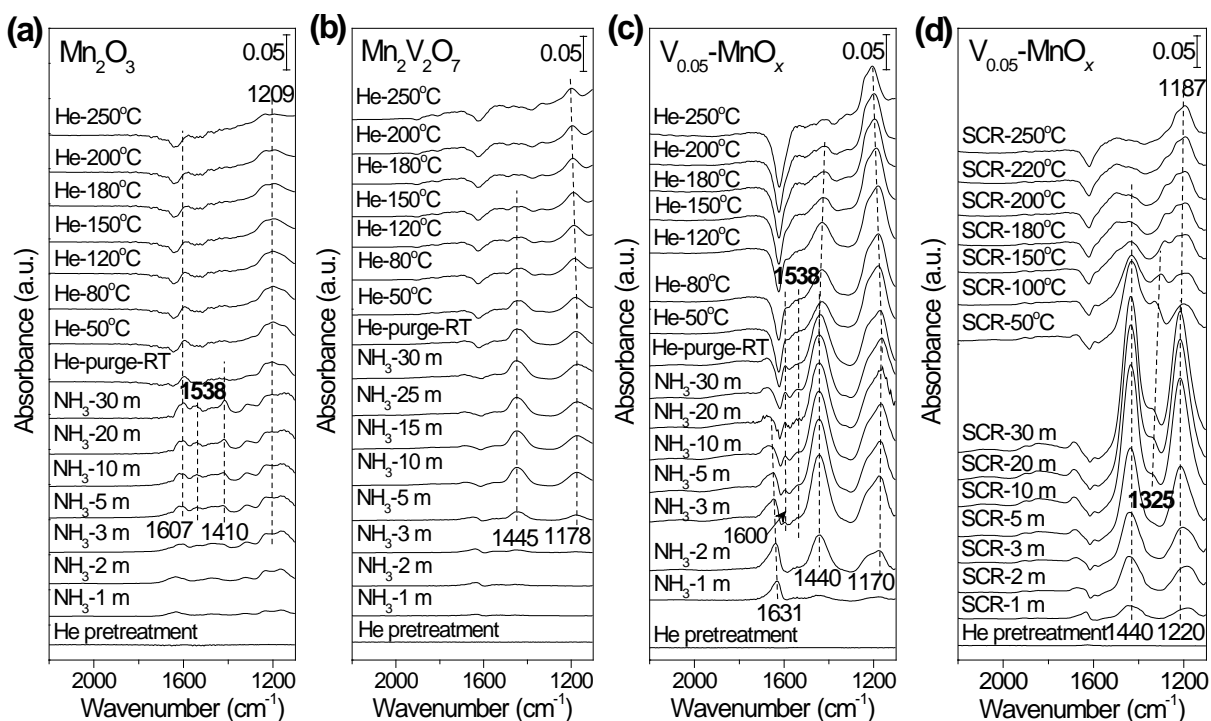
305

306 **Figure 6.** *In situ* IR spectra of (a-c), NH$_3$ adsorption at steady-state and (d) during SCR reaction

307 over (a) Mn$_2$O$_3$, (b) Mn$_2$V$_2$O$_7$ and (c, d) V$_{0.05}$-MnO$_x$.

308

309 To investigate the nature of the adsorbed NH$_3$ species and potential reaction intermediates, *in*

310 *situ* IR spectra were collected of NH$_3$ adsorption at room temperature and subsequent desorption

311 with increasing temperature (Figure 6a-c). Only ammonia adsorption at Lewis acid sites was

18

312   observed for Mn_2O_3 (Figure 6a), which is supported by the absence of negative bands about 3600

313   cm^{-1} (Figure S6a).[45,71-73] Bands at ~1209 and ~1607 cm^{-1} are attributed to the symmetric and

314   asymmetric bending modes of NH_3 coordinately linked to Lewis acid sites, respectively.[72] The

315   weak band at 1410 cm^{-1} disappears completely after He purging at room temperature, which is

316   derived from the protonation of weakly adsorbed NH_3.[29] Notably, a band at 1538 cm^{-1} was

317   observed for Mn_2O_3, which is attributed to the scissoring vibration mode of weakly adsorbed

318   NH_2 (amide) species arising from the partial oxidation of NH_3 (H-abstraction),[74] because it

319   disappears after the He purge at room temperature.[72]

320   In addition, for $Mn_2V_2O_7$, evidence for both Brønsted and Lewis acid sites was observed from

321   Figure 6b, while the IR spectra of $V_{0.05}$-MnO_x exhibits the combined characteristics of Mn_2O_3

322   and $Mn_2V_2O_7$ (Figure S6b and 6c). The bands at 3353-3028 cm^{-1} arise from N-H stretching

323   vibrations of NH_3 adsorbed on Lewis sites (Figure S6b). The corresponding bending vibrations

324   are observed at 1170/1178 cm^{-1} (Figure 6c).[75-77] The characteristic bands for NH_4^+ formed by the

325   interaction of NH_3 with Brønsted sites around 1440 cm^{-1} (Figure 6c) are also supported by the

326   negative band at 3660-3670 cm^{-1} (Figure S6b), which indicates the consumption of the -OH. The

327   enhanced quantities of Lewis and Brønsted acidity in $V_{0.05}$-MnO_x compared with those of Mn_2O_3

328   and $Mn_2V_2O_7$ are again potentially indicative of synergistic effects between the components, in

329   accordance with the NH_3-TPD results (Figure 5b and Table 1). In addition, NH_3 bound to Lewis

330   acid sites were more strongly adsorbed,[72] because the intensity of bands due to Brønsted acid

331   sites decreased noticeably with the increasing temperature, while those due to adsorption at

332   Lewis acid sites still remained. Importantly, the NH_2 species at 1538 cm^{-1} was still detected in

333   $V_{0.05}$-MnO_x. In comparison with *in situ* IR spectra of the MoO_3+$Mn_2V_2O_7$ sample (which lacks

334   redox properties at low temperature) (Figure S7), it is concluded that the NH_2 species arose from

335   the activation of the adsorbed NH_3 on Mn_2O_3. Moreover, despite the high amount of Brønsted

336   acidity in the $MoO_3+Mn_2V_2O_7$ sample, its poor SCR activity may indicate that the Lewis acidity

337   may play a crucial role in the SCR reaction at low temperature (Figure 3 and Figure S7).[24]

338   **4.4 Transfer of reaction intermediates and reaction mechanism**
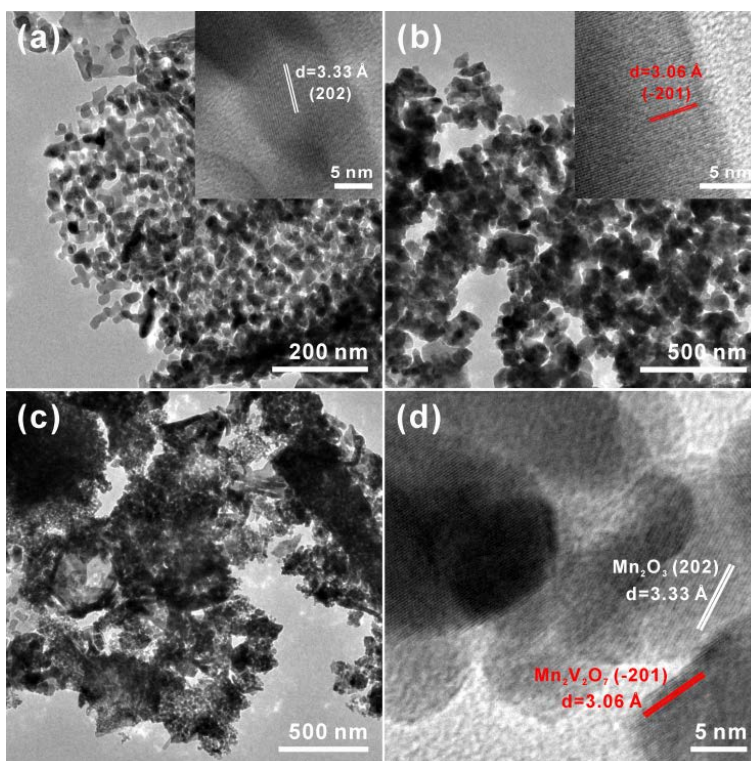
340   **Figure 7.** TEM and HRTEM images of (a) Mn_2O_3, (b) $Mn_2V_2O_7$, (c, d) $V_{0.05}$-MnO_x.

342   TEM characterization reveals that the nanoparticles are aggregated together with ~20 (Figure

343   7a) and ~80 nm in diameter (Figure 7b) for Mn_2O_3 and $Mn_2V_2O_7$, respectively. The close

344   proximity of Mn_2O_3 and $Mn_2V_2O_7$ particles in V_a-MnO_x is demonstrated in the example of $V_{0.05}$-

345   MnO_x (Figure 7c and d). This again may be seen as evidence that the higher activity of V_a-MnO_x

346   compared with Mn_2O_3 which contributes to the synergism between Mn_2O_3 and $Mn_2V_2O_7$. It is

347 likely that the NH_2 intermediate from NH_3 partial oxidation on Mn_2O_3 transfers to $Mn_2V_2O_7$

348 where the further reactions of NH_2 with gaseous NO ultimately produce N_2 rather than N_2O over

349 Mn_2O_3. Following this assumption, it could be the case that $V_{0.05}$-MnO_x, which shows the

350 maximum activity, exhibits the optimal contact between Mn_2O_3 and $Mn_2V_2O_7$, thus facilitating

351 transfer of intermediates. According to the physical dimensions of Mn_2O_3 and $Mn_2V_2O_7$

352 nanoparticles in V_a-MnO_x, the optimal ratio of Mn_2O_3 and $Mn_2V_2O_7$ is calculated by assuming

353 that the particles are spherical and tangentially contacted (Figure 8). At most, one hundred

354 Mn_2O_3 spherical particles are at a tangent with the surface of one $Mn_2V_2O_7$ particle, while for

355 one Mn_2O_3 spherical particle, only 6.25 $Mn_2V_2O_7$ particles are located at its external surface

356 tangentially. Therefore, the calculated optimal matching value for the molar ratio between

357 Mn_2O_3 and $Mn_2V_2O_7$ is 16, which is very close to those of the calculated molar ratios from

358 theoretical values and quantitative XRD analysis for $V_{0.05}$-MnO_x (Table 1). This confirms that

359 the optimal activity of $V_{0.05}$-MnO_x is a consequence of the optimal contact arising between the

360 two components which facilitate the transfer of the active intermediates. Anyway, the transfer

361 process will be corroborated by the following DFT calculations.
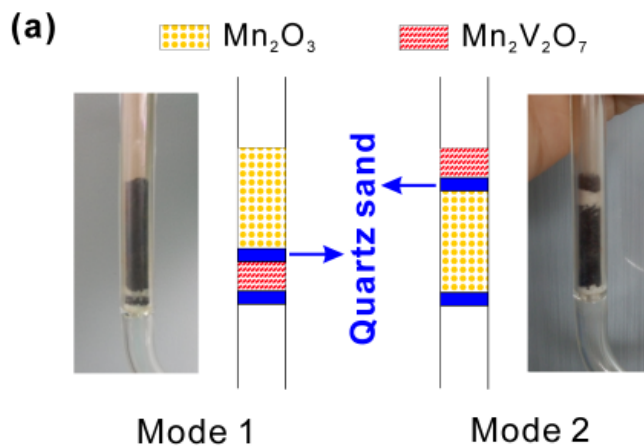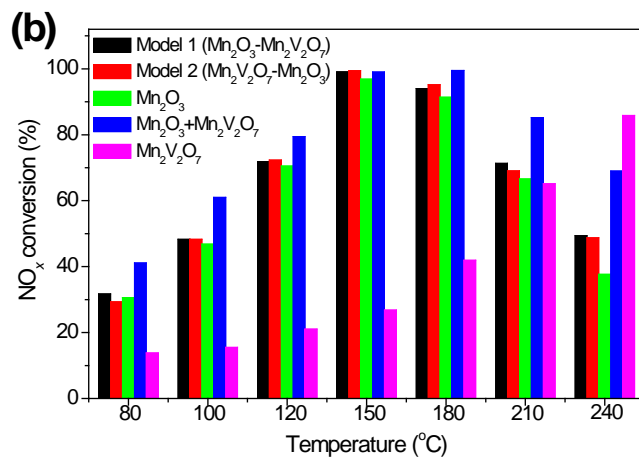
362
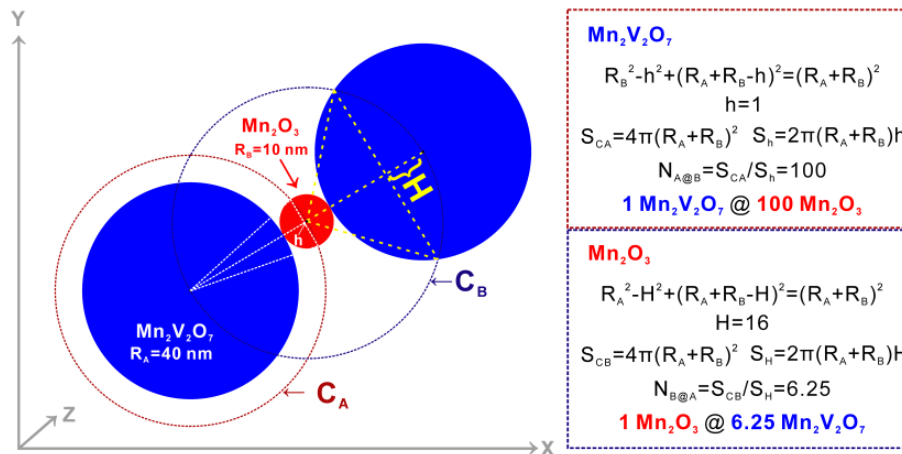
363

364   **Figure 8.** The simulated geometric configuration and calculation formulas for the optimal

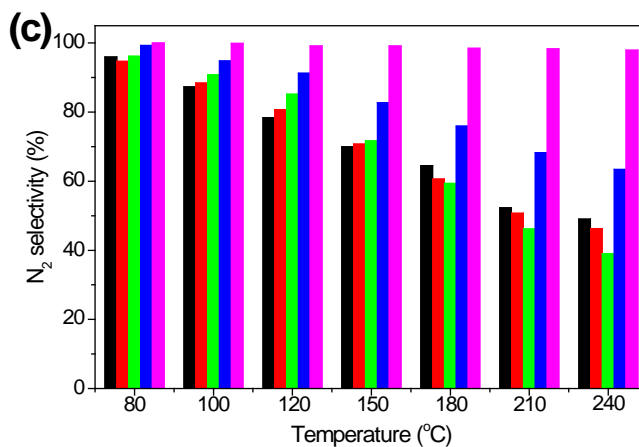365   contact between the two different phases.

366

367

368

369

370   **Figure 9.** (a) Photographs and schematic graphs of Mode 1 and 2, (b) NO_x conversion and (c) N_2

371   selectivity of the Mode 1 and 2 samples. Dual-bed configuration with Mn_2O_3 packed above

372   (Mode 1) or below (Mode 2) $Mn_2V_2O_7$ and separated by a layer of quartz sand.

373

374   To further demonstrate the transfer of the reactive intermediate, SCR reactions over the

375 catalysts with the two functionalities packed in different modes under the same conditions were

376 performed (Figure 9a). Irrespective of Mode 1 or 2, the negligible improvement in activity was

377 observed compared with Mn_2O_3 (Figure 9b and c) indicating that even though the active

378 intermediates are generated over Mn_2O_3, transfer cannot proceed (Mode 1) due to the long-

379 distance between the two components. In addition, the activity of the $Mn_2O_3+Mn_2V_2O_7$ sample is

380 higher than those of Mode 1 and 2 (Figure 9b and c), confirming that tight contact is

381 indispensable, as in the case of V_a-MnO_x.

382   Further investigation of the transferred NH_2 from Mn_2O_3 with gaseous NO on $Mn_2V_2O_7$ was

383 conducted using *in situ* IR spectra of the SCR reaction over $V_{0.05}$-MnO_x (Figure 6d). In

384 comparison with Figure 6c, a unique band at ~1325 cm^{-1} which was not found over pure Mn_2O_3

385 and $Mn_2V_2O_7$ samples could be attributed to N=O stretching vibration. However, in the surface

386 reactions on $V_{0.05}$-MnO_x between not only $NO+O_2$ and pre-adsorbing NH_3 (Figure S8a) but also

387 NH_3 and pre-adsorbed $NO+O_2$ (Figure S8b), the ~1325 cm^{-1} band is similarly present, suggesting

388 that it is correlated with both N=O and N-H moieties, most likely due to the NH_2NO species,[78]

389 arising from the combination of the NH_2 species and gaseous NO.[72] This assignment will be

390 shown reasonable by DFT calculations. Thus, the V_a-MnO_x system works as a bifunctional

391 catalyst, in which Mn_2O_3 is responsible for NH_3 activation while $Mn_2V_2O_7$ participates in N_2

23

392   production whilst the transfer of the NH_2 intermediate occurs between the two components.

393   Without NH_2 migration from Mn_2O_3 to $Mn_2V_2O_7$, this NH_2 intermediate would be further

394   oxidized to N_2O over the Mn_2O_3. Once NH_2 intermediate is transferred to $Mn_2V_2O_7$, the NH_2NO

395   formed over $Mn_2V_2O_7$ is converted to N_2 rather than N_2O at lower temperature. To verify the

396   above hypothesis, DFT calculations were performed.

397   **4.5 DFT calculations**

398   As displayed in HRTEM images (the insets of Figure 7a and b), the (202) and ($\bar{2}$01) surfaces

399   were exposed for Mn_2O_3 and $Mn_2V_2O_7$, respectively. Consequently, DFT calculation was carried

400   out on Mn_2O_3(202) (Figure S9) and $Mn_2V_2O_7$($\bar{2}$01) (Figure S10). Other considerations for

401   choosing the two facets are provided in Supporting Information.

402   Firstly, the calculations of NH_3 adsorption were conducted and the corresponding adsorption

403   energies of the most stable configuration (Figure S11) on Mn_2O_3(202) and $Mn_2V_2O_7$($\bar{2}$01) are

404   listed in Table S1. The adsorption energies were calculated on the basis of PBE+U and checked

405   by HSE06 calculations. As listed in Table S1, PBE+U and HSE06 results are qualitatively

406   consistent. In the case of Mn_2O_3, NH_3 tends to adsorb atop at the Lewis acid sites of Mn_{4c}^{I} (4-fold

407   coordinated Mn cation) rather than at the Brønsted site of HO_{2c}^{I} (two-fold coordinated oxygen

408   anion) over Mn_2O_3(202). Moreover, the adsorption energy of NH_3 is evidently stronger than that

409   of NO over Mn_2O_3(202), suggesting that the Lewis acid site of Mn would be occupied by NH_3

410   while NO is difficult to adsorb on the surface. In the case of $Mn_2V_2O_7$, NH_3 also preferentially

411   adsorbs at the Lewis acid site of Mn_{5c}^{I} (Mn_{5c}^{I} 5-fold coordinated Mn cation) rather than at the

412   Brønsted site of HO_{1c}(one-fold coordinated oxygen anion) over $Mn_2V_2O_7$($\bar{2}$01). Nevertheless,

413   the adsorption strength of NH_3 over $Mn_2V_2O_7$($\bar{2}$01) is weaker than that over Mn_2O_3(202) at

414 Lewis acid sites while the order of NH_3 binding strength is reversed at Brønsted site due to the

415 existence of one-fold coordinated oxygen at $Mn_2V_2O_7(\bar{2}01)$. These facts imply a stronger Lewis

416 acidity of Mn cations at the $Mn_2O_3(202)$ surface compared with those in the $Mn_2V_2O_7(\bar{2}01)$

417 surface. In addition, NO barely adsorbs over $Mn_2V_2O_7(\bar{2}01)$, which suggests that the Lewis acid

418 sites would also be occupied by NH_3 on the $Mn_2V_2O_7(\bar{2}01)$ surface. The above results are all in

419 good agreement with the *in situ* IR characterization.

420
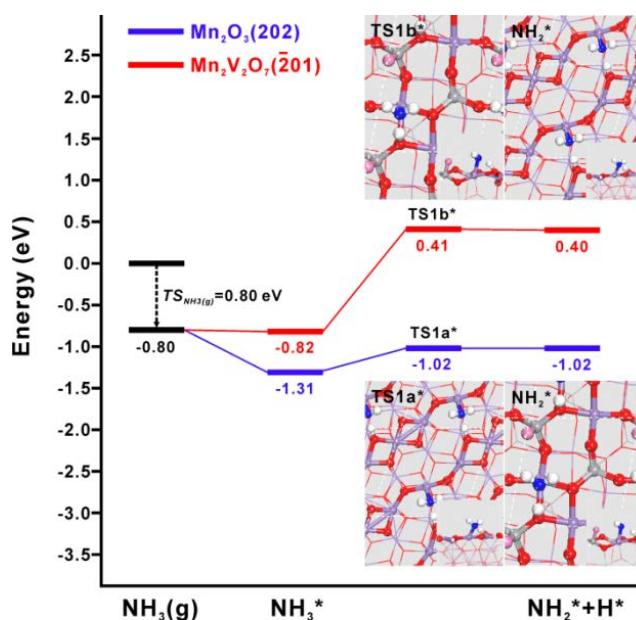
421

422 **Figure 10.** Energy profiles of NH_3 adsorption and its oxidative dehydrogenation over

423 $Mn_2O_3(202)$ and $Mn_2V_2O_7(\bar{2}01)$ considering the large entropy of gaseous NH_3 ($T = 400$ K, $TS =$

424 0.80 eV) and the corresponding transition state structures of TS1a* and TS1b* and final states of

425 adsorbed NH_3* oxidative dehydrogenation over these two surfaces, respectively.

426

427   Since NH_3 exposure prior to NO adsorbs at Lewis acid sites over both Mn_2O_3(202) and

428       $Mn_2V_2O_7$($\bar{2}$01), we further explored NH_3 oxidative dehydrogenation over Mn_2O_3(202) and

429       $Mn_2V_2O_7$($\bar{2}$01) at a reaction temperature of 400 K. As shown in Figure 10, not only is the

430   adsorption strength of NH_3 on Mn_2O_3(202) stronger than on $Mn_2V_2O_7$($\bar{2}$01) but also the NH_3

431   activation barrier of 0.29 eV on Mn_2O_3(202) is much lower in comparison with 1.23 eV for

432       $Mn_2V_2O_7$($\bar{2}$01), indicating that Mn_2O_3 with excellent oxidation properties can readily activate the

433   adsorbed NH_3 to form $NH_2^*+H^*$ (* denotes the adsorbed species) which is demanding on

434       $Mn_2V_2O_7$($\bar{2}$01).

435
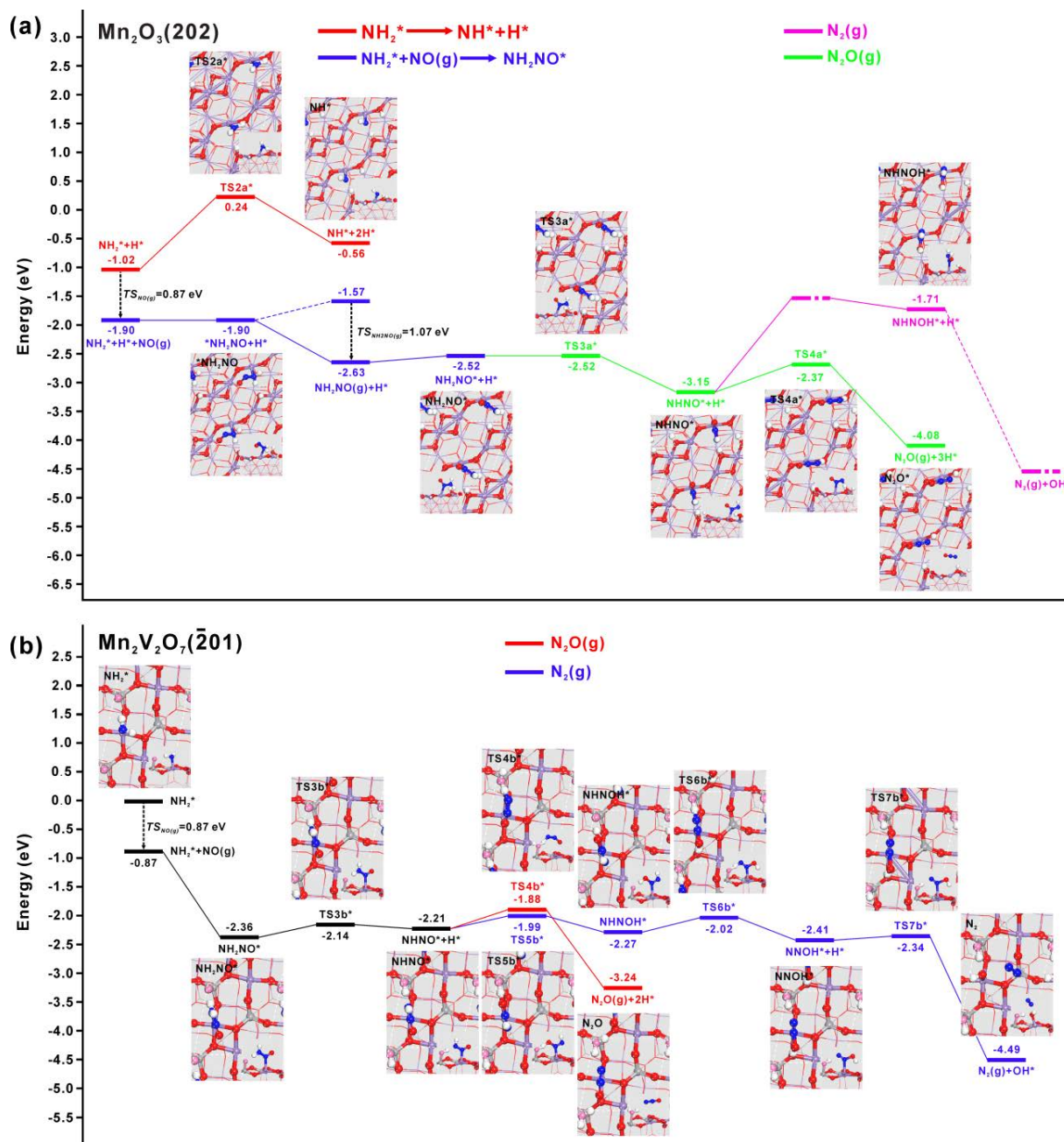
Figure 11. (a) Energy profiles and the corresponding transition states and intermediate states geometry structures of the oxidative dehydrogenation of NH_2* and the formation of N_2O and N_2 processes over $Mn_2O_3(202)$ considering the great entropy of gaseous NO and NH_2NO (T = 400 K, TS_{NO} = 0.87 eV and TS_{NH_2NO} = 1.07 eV); (b) Energy profiles and the corresponding transition states and intermediate states geometry structures of N_2O and N_2 formation over $Mn_2V_2O_7(\bar{2}01)$

442   after the migration of NH_2^* from $Mn_2O_3(202)$ to $Mn_2V_2O_7(\bar{2}01)$ considering the great entropy of

443   gaseous NO and NH_2NO ($T = 400$ K, $TS_{NO} = 0.87$ eV).

444

445   Accordingly, the subsequent reaction channels beginning with NH_2^* including the possible

446   further oxidative dehydrogenation of NH_2^* were investigated over $Mn_2O_3(202)$. As shown in

447   Figure 11a, on the one hand, the energy barrier for NH_2^* oxidative dehydrogenation to NH^* is as

448   high as 1.26 eV, leading to the outcome that the formation of NH^*+2H^* from activated $NH_2^*+H^*$

449   via this pathway, i.e. the deep oxidative dehydrogenation of NH_3 would not be feasible at low

450   temperature. On the other hand, the formation of $^*NH_2NO$ from NH_2^* and gaseous NO is

451   evidently exothermic, which could compensate for the entropy loss of gaseous NO due to its

452   fixation by the surface. This indicates that NH_2^* tends to associate with gaseous NO to produce

453     $^*NH_2NO$ rather than undergo further dehydrogenation. After the desorption and re-adsorption

454   process, the chemisorption of $^*NH_2NO$ at Mn site will switch from the configuration via the N of

455   NH_2 moiety to the more stable configuration via the N of NO moiety ($^*NH_2NO \rightarrow NH_2NO^*$). The

456   NH_2NO^* formed could then be dehydrogenated to $NHNO^*$ almost without energy barrier which

457   then tends to be further dehydrogenated to form N_2O instead of the more desirable N_2 from the

458   dehydroxylation over $Mn_2O_3(202)$. The formation of N_2 must undergo N-O bond dissociation

459   process. Since the breaking of the single bond of N-O in NHNOH and the formation of

460   monovalent NHN^* and OH^* would be thermodynamically far easier than the breaking of double

461   bond of N=O in NHNO and the formation of bivalent NH_2N^* and O^* with stronger bonding

462   competition at single Mn cation of $Mn_2O_3(202)$, the production of N_2 will pass through

463     $NHNOH^*$ over $Mn_2O_3(202)$. However, since the reaction energy from $NHNO^*$ to $NHNOH^*$ is

464   1.44 eV, which is even higher than the energy barrier of 0.78 eV for the dehydrogenation of

465   NHNO* to yield N_2O, N_2O production is more favorable than N_2 over the pure $Mn_2O_3(202)$

466   surface. This DFT result is consistent with the experimental results of the low N_2 selectivity of

467   Mn_2O_3 in SCR reaction (Figure 3b).

468   Interestingly, in the presence of the second component of $Mn_2V_2O_7$, despite the tough

469   oxidative dehydrogenation of NH_3 to produce NH_2^* over $Mn_2V_2O_7(\bar{2}01)$, once NH_2^* is able to

470   migrate to this surface from the $Mn_2O_3(202)$ surface, it is clear from Figure 11b that the energy

471   barriers of the subsequent reaction channels towards the production of N_2O and N_2 are all rather

472   low. Additionally, although the facile energy barrier of oxidative dehydrogenation of NHNO* to

473   yield N_2O over $Mn_2V_2O_7(\bar{2}01)$ (0.33 eV) is evidently lower than that over $Mn_2O_3(202)$ (0.78

474   eV), the energy barriers in the branch pathway towards the formation of gaseous N_2 starting from

475   NHNO* are all even lower than the energy barrier of N_2O formation over $Mn_2V_2O_7(\bar{2}01)$. This

476   might be attributed to the presence of one-fold coordinated lattice oxygen anion at the surface of

477      $Mn_2V_2O_7(\bar{2}01)$ with stronger Lewis basicity and steric structure advantage which is in favor of

478   the hydrogen transfer between the surface and intermediates via hydrogen bond for the formation

479   of NHNOH* and NNOH*. Thus N_2 production is more favorable than N_2O over $Mn_2V_2O_7(\bar{2}01)$

480   surface. Furthermore, once NH_2^* could readily migrate to $Mn_2V_2O_7$ from Mn_2O_3, the formation

481   of N_2O over the $Mn_2O_3(202)$ surface could be suppressed. This sheds light on the fact that N_2

482   could be rapidly and selectively produced utilizing V_a-MnO_x catalysts, which also underscores

483   the significance of the existence of Mn_2O_3 which is capable of activating NH_3 to form NH_2^* and

484   the intimate contact between Mn_2O_3 and $Mn_2V_2O_7$ on which NH_2^* migration depends.

485   Combining experimental results with DFT calculations, we conclude that the SCR reaction

486   over this bifunctional catalyst mainly follows the pathway as described: adsorbed NH_3 is

487   activated over Mn_2O_3 into a NH_2 intermediate, which then transfers to $Mn_2V_2O_7$ where it reacts

488   with gaseous NO to form NH_2NO, which will be exclusively decomposed into N_2. The NO_x

489   conversion on Mn_2O_3 into N_2O is thus inhibited.

490

491   **5. CONCLUSIONS**

492   In summary, we have fabricated the bifunctional V_a-MnO_x catalysts composed of Mn_2O_3 and

493   $Mn_2V_2O_7$, which separate the activation of NH_3 and the production of N_2 via an active

494   intermediate NH_2 transfer. Both NO_x conversion and N_2 selectivity are greatly improved in

495   comparison with Mn_2O_3 at the low temperature due to the synergism between Mn_2O_3 and

496   $Mn_2V_2O_7$ which enhanced Lewis acid density of V_a-MnO_x. The maximum activity for $V_{0.05}$-

497   MnO_x is attributed to the optimal contact between these two components, highlighting the

498   significance of the proximity for transfer of the intermediate. Using a combination of *in situ* IR

499   characterization and DFT calculations, the NH_2 intermediate was found to be formed by NH_3

500   dehydrogenation over Mn_2O_3, and to subsequently be transferred and reacted with gaseous NO

501   into NH_2NO on $Mn_2V_2O_7$, which exclusively decomposes into N_2. The deep oxidation of

502   adsorbed NH_3 on Mn_2O_3 into N_2O is therefore inhibited.

503

504   **ASSOCIATED CONTENT**

505   **Supporting Information**. Additional characterization data (such as XAFS, Raman, XPS,

506   XRD and *in situ* IR) and theoretical calculation results can be found in the Supporting

507   Information.

508

509   AUTHOR INFORMATION

510   **Corresponding Author**

511   *chm_zhangzl@ujn.edu.cn

512   *xmcao@ecust.edu.cn

513   *j.anderson@abdn.ac.uk

514

522   **REFERENCES**

523   (1)   Centia, G.; Ciambelli, P.; Perathoner, S.; Russo, P. Environmental catalysis trends and outlook, *Catal.*
524   *Today* **2002**, 75, 3-15.

525   (2)   Liu, C.; Shi, J. W.; Gao, C.; Niu, C. M. Manganese oxide-based catalysts for low-temperature selective
526   catalytic reduction of NO_x with NH_3: A review, *Appl. Catal. A: Gen.* **2016**, 522, 54-69.

527   (3)   Kang, M.; Park, E. D.; Kim, J. M.; Yie, J. E. Manganese oxide catalysts for NO_x reduction with NH_3 at
528   low temperatures, *Appl. Catal. A: Gen.* **2007**, 327, 261-269.

529   (4)   Liu, Y.; Xu, J.; Li, H. R.; Cai, S. X.; Hu, H.; Fang, C.; Shi, L. Y.; Zhang, D. S. Rational design and *in situ*

530   fabrication of $MnO_2@NiCo_2O_4$ nanowire arrays on Ni foam as high-performance monolith de-NO_x

531   catalysts, *J. Mater. Chem. A* **2015**, 3, 11543-11553.

532   (5) Qi, G.; Yang, R. T.; Chang, R. MnO_x-CeO_2 mixed oxides prepared by co-precipitation for selective

533   catalytic reduction of NO with NH_3 at low temperatures, *Appl. Catal. B: Environ.* **2004**, 51, 93-106.

534   (6) Busca, G.; Lietti, L.; Ramis, G.; Berti, F. Chemical and mechanistic aspects of the selective catalytic

535   reduction of NO_x by ammonia over oxide catalysts: A review, *Appl. Catal. B: Environ.***1998**, 18, 1-36.

536   (7) Xiong, Y.; Tang, C. J.; Yao, X. J.; Zhang, L.; Li, L. L.; Wang, X. B.; Deng, Y.; Gao, F.; Dong, L. Effect of

537   metal ions doping (M=Ti^{4+}, Sn^{4+}) on the catalytic performance of MnO_x/CeO_2 catalyst for low

538   temperature selective catalytic reduction of NO with NH_3, *Appl. Catal. A: Gen.* **2015**, 495, 206-216.

539   (8) Liu, F. D.; Yu, Y. B.; He, H. Environmentally-benign catalysts for the selective catalytic reduction of NO_x

540   from diesel engines: structure-activity relationship and reaction mechanism aspects, *Chem. Commun.*

541   **2014**, 50, 8445-8463.

542   (9) Li, J. H.; Chang, H. Z.; Ma, L.; Hao, J. M.; Yang, R. T. Low-temperature selective catalytic reduction of

543   NO_x with NH_3 over metal oxide and zeolite catalysts—A review, *Catal. Today* **2011**, 175, 147-156.

544 (10) Zhang, S. G.; Zhang, B. L.; Liu, B.; Sun, S. L. A review of Mn-containing oxide catalysts for low

545   temperature selective catalytic reduction of NO_x with NH_3: reduction mechanism and catalyst

546   deactivation, *RSC Adv.* **2017**, 7, 26226-26242.

547 (11) Tang, X. F.; Li, J. H.; Sun, L.; Hao, J. M. Origination of N_2O from NO reduction by NH_3 over β-MnO_2

548   and α-Mn_2O_3, *Appl. Catal. B: Environ.* **2010**, 99, 156-162.

549 (12) Tang, X. F.; Hao, J. M.; Xu, W. G.; Li, J. H. Low temperature selective catalytic reduction of NO_x with

550   NH_3 over amorphous MnO_x catalysts prepared by three methods, *Catal. Commun.* **2007**, 8, 329-334.

551 (13) Tian, W.; Yang, H. S.; Fan, X. Y.; Zhang, X. B. Catalytic reduction of NO_x with NH_3 over different-

552   shaped MnO_2 at low temperature, *J. Hazard. Mater.* **2011**, 188, 105-109.

553 (14) Xu, H. M.; Yan, N. Q.; Qu, Z.; Liu, W.; Mei, J.; Huang, W. J.; Zhao, S. J. Gaseous heterogeneous catalytic

554   reactions over Mn-based oxides for environmental applications: A critical review, *Environ. Sci. Technol.*

555   **2017**, 51, 8879-8892.

556 (15) Long, R. Q.; Yang, R. T.; Chang, R. Low temperature selective catalytic reduction (SCR) of NO with NH_3

557   over Fe-Mn based catalysts, *Chem. Commun.* **2002**, 452-453.

558   (16) Qi, G.; Yang, R. T. Performance and kinetics study for low-temperature SCR of NO with NH_3 over MnO_x-

559   CeO_2 catalyst, *J. Catal.* **2003**, 217, 434-441.

560   (17) Eigenmann, F.; Maciejewski, M.; Baiker, A. Selective reduction of NO by NH_3 over manganese-cerium

561   mixed oxides: Relation between adsorption, redox and catalytic behavior, *Appl. Catal. B: Environ.* **2006**,

562   62, 311-318.

563   (18) Casapu, M.; Krocher O.; Elsener, M. Screening of doped MnO_x–CeO_2 catalysts for low-temperature NO-

564   SCR, *Appl. Catal. B: Environ.* **2009**, 88, 413-419.

565   (19) Wan, Y. P.; Zhao, W. R.; Tang, Y.; Li, L.; Wang, H. J.; Cui, Y. L.; Gu, J. L.; Li, Y. S.; Shi, J. L. Ni-Mn bi-

566   metal oxide catalysts for the low temperature SCR removal of NO with NH_3, *Appl. Catal. B: Environ.*

567   **2014**, 148-149, 114-122.

568   (20) Lian, Z. H.; Liu, F. D.; He, H.; Shi, X. Y.; Mo, J. S.; Wu, Z. B. Manganese-niobium mixed oxide catalyst

569   for the selective catalytic reduction of NO_x with NH_3 at low temperatures, *Chem. Eng. J.* **2014**, 250, 390-

570   398.

571   (21) Chen, Z. H.; Yang, Q.; Li, H.; Li, X. H.; Wang, L. F.; Tsang, S. C. Cr-MnO_x mixed-oxide catalysts for

572   selective catalytic reduction of NO_x with NH_3 at low temperature, *J. Catal.* **2010**, 276, 56-65.

573   (22) Zuo, J. L.; Chen, Z. H.; Wang, F. R.; Yu, Y. H.; Wang, L. F.; Li, X. H. Low-temperature selective catalytic

574   reduction of NO_x with NH_3 over novel Mn−Zr mixed oxide catalysts, *Ind. Eng. Chem. Res.* **2014**, 53,

575   2647-2655.

576   (23) Qi, G.; Yang, R. T. Low-temperature selective catalytic reduction of NO with NH_3 over iron and

577   manganese oxides supported on titania, *Appl. Catal. B: Environ.* **2003**, 44, 217-225.

578   (24) Smirniotis, P. G.; Peña, D. A.; Uphade, B. S. Low-temperature selective catalytic reduction (SCR) of NO

579   with NH_3 by using Mn, Cr, and Cu oxides supported on hombikat TiO_2, *Angew. Chem. Int. Ed.* **2001**, 40,

580   2479-2482.

581   (25) Smirniotis, P. G.; Sreekanth, P. M.; Peña, D. A.; Jenkins, R. G. Manganese oxide catalysts supported on

582   TiO_2, Al_2O_3, and SiO_2: A comparison for low-temperature SCR of NO with NH_3, *Ind. Eng. Chem. Res.*

583   **2006**, 45, 6436-6443.

584   (26) Park, E.; Kim, M.; Jung, H.; Chin, S.; Jurng, J. Effect of sulfur on Mn/Ti catalysts prepared using

585   chemical vapor condensation (CVC) for low-temperature NO reduction, *ACS Catal.* **2013**, 3, 1518-1525.

586   (27) Huang, J. H.; Tong, Z. Q.; Huang, Y.; Zhang, J. F. Selective catalytic reduction of NO with NH$_3$ at low

587   temperatures over iron and manganese oxides supported on mesoporous silica, *Appl. Catal. B: Environ.*

588   **2008**, 78, 309-314.

589   (28) Singoredjo, L.; Korver, R.; Kapteijn, F.; Moulijn, J. Alumina supported manganese oxides for the low-

590   temperature selective catalytic reduction of nitric oxide with ammonia, *Appl. Catal. B: Environ.* **1992**, 1,

591   297-316.

592   (29) Kapteijn, F.; Singoredjo, L.; Driel, M.; Andreini, A.; Moulijn, J. A.; Ramis, G.; Busca, G. Alumina-

593   supported manganese oxide catalysts: II. Surface characterization and adsorption of ammonia and nitric

594   oxide, *J. Catal.* **1994**, 150, 106-115.

595   (30) Qi, G.; Yang, R. T.; Chang, R. Low-temperature SCR of NO with NH$_E$ over USY-supported manganese

596   oxide-based catalysts, *Catal. Lett.* **2003**, 87, 67-71.

597   (31) Lou, X. R.; Liu, P. F.; Li, J.; Li, Z.; He, K. Effects of calcination temperature on Mn species and catalytic

598   activities of Mn/ZSM-5 catalyst for selective catalytic reduction of NO with ammonia, *Appl. Surf. Sci.*

599   **2014**, 307, 382-387.

600   (32) Carja, G.; Kameshima, Y.; Okada, K.; Madhusoodana, C. D. Mn–Ce/ZSM5 as a new superior catalyst for

601   NO reduction with NH$_3$, *Appl. Catal. B: Environ.* **2007**, 73, 60-64.

602   (33) Marbán, G.; Valdés-Solís, T.; Fuertes, A. B. Mechanism of low-temperature selective catalytic reduction

603   of NO with NH$_3$ over carbon-supported Mn$_3$O$_4$ Role of surface NH$_3$ species: SCR mechanism, *J. Catal.*

604   **2004**, 226, 138-155.

605   (34) Wang, L. S.; Huang, B. C.; Su, Y. X.; Zhou, G. Y.; Wang, K. L.; Luo, H. C.; Ye, D. Q. Manganese oxides

606   supported on multi-walled carbon nanotubes for selective catalytic reduction of NO with NH$_3$: Catalytic

607   activity and characterization, *Chem. Eng. J.* **2012**, 192, 232-241.

608   (35) Fang, C.; Zhang, D. S.; Cai, S. X.; Zhang, L.; Huang, L.; Li, H. R.; Maitarad, P.; Shi, L. Y.; Gao, R. H.;

609   Zhang, J. P. Low-temperature selective catalytic reduction of NO with NH$_3$ over nanoflaky MnO$_x$ on

610   carbon nanotubes in situ prepared via a chemical bath deposition route, *Nanoscale*, **2013**, 5, 9199-9207.

611 (36) Xiao, X.; Sheng, Z. Y.; Yang L.; Dong, F. Low-temperature selective catalytic reduction of NO_x with NH_3

612 over a manganese and cerium oxide/graphene composite prepared by a hydrothermal method, *Catal. Sci.*

613 *Technol.* **2016**, 6, 1507-1514.

614 (37) Zhang, R. D.; Liu, N.; Luo, Z.; Yang, W.; Liang, X.; Xu, R. N.; Chen, B. H.; Duprez, D.; Royer, S. A

615 remarkable catalyst combination to widen the operating temperature window of the selective catalytic

616 reduction of NO by NH_3, *ChemCatChem* **2014**, 6, 2263-2269.

617 (38) Salazar, M.; Becker, R.; Grünert, W. Hybrid catalysts–an innovative route to improve catalyst

618 performance in the selective catalytic reduction of NO by NH_3, *Appl. Catal. B: Environ.* **2015**, 165, 316-

619 327.

620 (39) Salazar, M.; Hoffmann, S.; Tkachenko, O. P.; Becker, R.; Grünert, W. Hybrid catalysts for the selective

621 catalytic reduction (SCR) of NO by NH_3. On the role of fast SCR in the reaction network, *Appl. Catal. B:*

622 *Environ.* **2016**, 182, 213-219.

623 (40) Krivoruchenko, D. S.; Telegina, N. S.; Bokarev, D. A.; Stakheev, A. Y. Mn–Ce/beta "bifunctional"

624 catalyst for the selective catalytic reduction of nitrogen oxides with ammonia, *Kinet. Catal.* **2015**, 56,

625 741-746.

626 (41) Krivoruchenko, D. S.; Kucherov, A. V.; Telegina, N. S.; Bokarev, D. A.; Selvam, P.; Stakheev, A. Y.

627 Development of the bifunctional catalyst Mn-Fe-Beta for selective catalytic reduction of nitrogen oxides,

628 *Russ. Chem. B.* **2014**, 63, 389-395.

629 (42) Stakheev, A. Y.; Mytareva, A. I.; Bokarev, D. A.; Baeva, G. N.; Krivoruchenko, D. S.; Kustov, A. L.; Grill,

630 M.; Thøgersen, J. R. Combined catalytic systems for enhanced low-temperature NO_x abatement, *Catal.*

631 *Today* **2015**, 258, 183-189.

632 (43) Tang, X. L.; Li, Y. Y.; Yi, H. H.; Yu, Q. J.; Gao, F. Y.; Zhang, R. C.; Li, C. L.; Chu, C. An efficient two-

633 step method for NH_3 removal at low temperature using CoO_x-CuO_x/TiO_2 as SCO catalyst followed by

634 $NiMn_2O_4$ as SCR catalyst, *Energ. Fuel.* **2017**, 31, 8580-8593.

635 (44) Zhu, M. H.; Lai, J. K.; Tumuluri, U.; Wu, Z. L.; Wachs, I. E. Nature of active sites and surface

636 intermediates during SCR of NO with NH_3 by supported V_2O_5-WO_3/TiO_2 catalysts, *J. Am. Chem. Soc.*

637 **2017**, 139, 15624-15627.

638　(45) Vuong, T. H.; Radnik, J.; Rabeah, J.; Bentrup, U.; Schneider, M.; Atia, H.; Armbruster, U.; Grünert, W.;
639　　　Brückner, A. Efficient $VO_x/Ce_{1-x}Ti_xO_2$ catalysts for low-temperature NH_3-SCR: Reaction mechanism and
640　　　active sites assessed by in situ/operando spectroscopy, *ACS Catal.* **2017**, 7, 1693-1705.

641　(46) Huang, L.; Zhao, X.; Zhang, L.; Shi, L. Y.; Zhang, J. P.; Zhang, D. S. Large-scale growth of hierarchical
642　　　transition-metal vanadate nanosheets on metal meshes as monolith catalysts for De-NO_x reaction,
643　　　*Nanoscale* **2015**, 7, 2743-2749.

644　(47) Liu, F. D.; He, H.; Lian, Z. H.; Shan, W. P.; Xie, L. J.; Asakura, K.; Yang, W. W.; Deng, H. Highly
645　　　dispersed iron vanadate catalyst supported on TiO_2 for the selective catalytic reduction of NO_x with NH_3,
646　　　*J. Catal.* **2013**, 307, 340-351.

647　(48) Casanova, M.; Nodari, L.; Sagar, A.; Schermanz, K.; Trovarelli, A. Preparation, characterization and NH_3-
648　　　SCR activity of $FeVO_4$ supported on TiO_2-WO_3-SiO_2, *Appl. Catal. B: Environ.* **2015**, 176-177, 699-708.

649　(49) Zhao, X.; Huang, L.; Li, H.; Hu, H.; Hu, X. N.; Shi, L. Y.; Zhang, D. S. Promotional effects of zirconium
650　　　doped $CeVO_4$ for the low-temperature selective catalytic reduction of NO_x with NH_3, *Appl. Catal. B:*
651　　　*Environ.* **2016**, 183, 269-281.

652　(50) Marberger, A.; Elsener, M.; Ferri, D.; Sagar, A.; Schermanz, K.; Kröcher, O. Generation of NH_3 selective
653　　　catalytic reduction active catalysts from decomposition of supported $FeVO_4$, *ACS Catal.* **2015**, 5, 4180-
654　　　4188.

655　(51) Wu, G. X.; Li, J.; Fang, Z. T.; Lan, L.; Wang, R.; Gong, M. C.; Chen, Y. Q. $FeVO_4$ nanorods supported
656　　　TiO_2 as a superior catalyst for NH_3–SCR reaction in a broad temperature range, *Catal. Commun.* **2015**,
657　　　64, 75-79.

658　(52) Casanova, M.; Schermanz, K.; Llorca, J.; Trovarelli, A. Improved high temperature stability of NH_3-SCR
659　　　catalysts based on rare earth vanadates supported on TiO_2–WO_3–SiO_2, *Catal. Today* **2012**, 184, 227-236.

660　(53) Salazar, M.; Hoffmann, S.; Tillmann, L.; Singer, V.; Becher, R. Hybrid catalysts for the selective catalytic
661　　　reduction (SCR) of NO by NH_3: Precipitates and physical mixtures, *Appl. Catal. B: Environ.* **2017**, 218,
662　　　793-802.

663　(54) Chung, F. H. Quantitative interpretation of X-ray diffraction patterns of mixtures. I. Matrix-flushing
664　　　method for quantitative multicomponent analysis, *J. Appl. Cryst.* **1974**, 7, 519-525.

665   (55) Newville, M. IFEFFIT: interactive XAFS analysis and FEFF fitting, *J. Synchrotron Radiat.* **2001**, 8, 322-

666   324.

667   (56) Kresse, G.; Furthmüller, J. Efficient iterative schemes for *ab initio* total-energy calculations using a plane-

668   wave basis set, *Phys. Rev. B* **1996**, 54, 11169-11186.

669   (57) Kresse, G.; Furthmüller, J. Efficiency of ab-initio total energy calculations for metals and semiconductors

670   using a plane-wave basis set, *Comp. Mater. Sci.* **1996**, 6, 15-50.

671   (58) Kresse, G.; Joubert, D. From ultrasoft pseudopotentials to the projector augmented-wave method, *Phys.*

672   *Rev. B* **1999**, 59, 1758-1775.

673   (59) Perdew, J. P.; Burke, K.; Ernzerhof, M. Generalized gradient approximation made simple, *Phys. Rev. Lett.*

674   **1996**, 77, 3865-3868.

675   (60) Grant, R. W.; Geller, S.; Cape, J. A.; Espinosa, G. P. Magnetic and crystallographic transitions in the α-

676   Mn_2O_3-Fe_2O_3 system, *Phys. Rev.* **1968**, 175, 686-695.

677   (61) Wang, L.; Maxisch, T.; Ceder, G. Oxidation energies of transition metal oxides within the GGA+U

678   framework, *Phys. Rev. B* **2006**, 73, 195107.

679   (62) He, Z. Z.; Ueda, Y. Magnetic properties of $Mn_2V_2O_7$ single crystals, *J. Solid State Chem.* **2008**, 181, 235-

680   238.

681   (63) Yan, Q. M.; Li, G.; Newhouse, P. F.; Yu, J.; Persson, K. A.; Gregoire, J. M.; Neaton, J. B. $Mn_2V_2O_7$: An

682   earth abundant light absorber for solar water splitting, *Adv. Energy Mater.* **2015**, 1401840.

683   (64) Michaelides, A.; Hu, P.; Alavi, A. Physical origin of the high reactivity of subsurface hydrogen in catalytic

684   hydrogenation, *J. Chem. Phys.* **1999**, 111, 1343-1345.

685   (65) Liu, Z. P.; Hu, P. General trends in the barriers of catalytic reactions on transition metal surfaces, *J. Chem.*

686   *Phys.* **2001**, 115, 4977-4980.

687   (66) Hu, W. D.; Lan, J. G.; Guo, Y.; Cao, X. M.; Hu, P. Active low-coordination lattice oxygen and cooperation

688   of multiple active sites, *ACS Catal.* **2016**, 6, 5508-5519.

689   (67) Heyd, J.; Scuseria, G. E. Efficient hybrid density functional calculations in solids: Assessment of the

690   Heyd-Scuseria-Ernzerhof screened Coulomb hybrid functional, *J. Chem. Phys.* **2004**, 121, 1187-1192.

691   (68) Li, P.; Xin, Y.; Li, Q.; Wang, Z. P.; Zhang, Z. L.; Zheng, L. R. Ce−Ti amorphous oxides for selective

692   catalytic reduction of NO with NH$_3$: Confirmation of Ce−O−Ti active sites, *Environ. Sci. Technol.* **2012**,

693   46, 9600-9605.

694 (69) Jeong, J.; Aetukuri, N.; Graf, T.; Schladt, T. D.; Samant, M. G.; Parkin, S. S. P. Suppression of metal-

695   insulator transition in VO$_2$ by electric field-induced oxygen vacancy formation, *Science*, **2013**, 339, 1402-

696   1405.

697 (70) Silversmit, G.; Depla, D.; Poelman, H.; Marin, G. B.; Gryse, R. D. Determination of the V2p XPS binding

698   energies for different vanadium oxidation states (V^{5+} to V^{0+}), *J. Electron Spectrosc.* **2004**, 135, 167-175.

699 (71) Topsøe, N. Y. Mechanism of the selective catalytic reduction of nitric oxide by ammonia elucidated by in

700   situ on-line Fourier transform infrared spectroscopy, *Science* **1994**, 265, 1217-1219.

701 (72) Chen, L.; Li, J. H.; Ge, M. F. DRIFT study on cerium−tungsten/titiania catalyst for selective catalytic

702   reduction of NO$_x$ with NH$_3$, *Environ. Sci. Technol.* **2010**, 44, 9590-9596.

703 (73) Centeno, M. A.; Carrizosa, I. Odriozola, J. A. NO–NH$_3$ coadsorption on vanadia/titania catalysts:

704   determination of the reduction degree of vanadium, *Appl. Catal. B: Environ.* **2001**, 29, 307-314.

705 (74) Liu, F. D.; He, H.; Zhang, C. B.; Shan, W. P.; Shi, X. Y. Mechanism of the selective catalytic reduction of

706   NO$_x$ with NH$_3$ over environmental-friendly iron titanate catalyst, *Catal. Today* **2011**, 175, 18-25.

707 (75) Amores, J. M. G.; Escribano, V. S.; Ramis, G.; Busca, G. An FT-IR study of ammonia adsorption and

708   oxidation over anatase-supported metal oxides, *Appl. Catal. B: Environ.* **1997**, 13, 45-58.

709 (76) Wu, Z. B.; Jiang, B. Q.; Liu, Y.; Wang, H. Q.; Jin, R. B. DRIFT study of manganese-titania-based

710   catalysts for low-temperature selective catalytic reduction of NO with NH$_3$, *Environ. Sci. Technol.* **2007**,

711   41, 5812-5817.

712 (77) Qi, G.; Yang, R. T. MnO$_x$-CeO$_2$ mixed oxides prepared by co-precipitation for selective catalytic

713   reduction of NO with NH$_3$ at low temperatures, *J. Phys. Chem. B* **2004**, 108, 15738-15747.

714 (78) Li, Q.; Gu, H. C.; Li, P.; Zhou, Y. H.; Liu, Y.; Qi, Z. N.; Xin, Y.; Zhang, Z. L. In situ IR studies of

715   selective catalytic reduction of NO with NH$_3$ on Ce-Ti amorphous oxides, *Chinese J. Catal.* **2014**, 35,

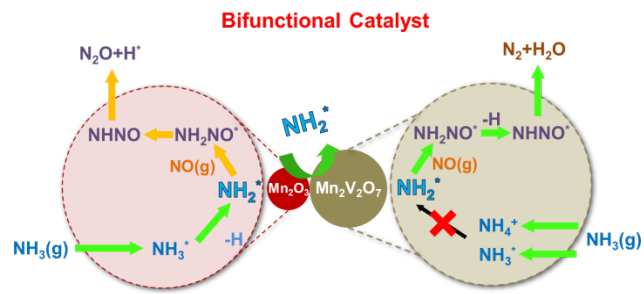716   1289-1298.

717

718

719

720

721

722

723

724

725

726

727

728

729

730

731

732 **Table of Contents**

733